

Computationally Efficient Radio Frequency Source Localisation for Radio Interferometric Arrays

Jan-Willem W. Steeb¹, David B. Davidson^{2,1}, and Stefan J. Wijnholds^{3,1}

¹Department of Electrical & Electronic Engineering, Stellenbosch University, South Africa

²Curtin Institute of Radio Astronomy (CIRA), Curtin University, Australia

³Netherlands Institute for Radio Astronomy (ASTRON), The Netherlands

Key Points:

- We present a source localisation algorithm for arbitrary arrays working in near-field and far-field
- The scaling of the algorithm is linear with search grid size instead of cubic as 3D MUSIC
- The accuracy of the algorithm is validated using simulations and data from the LOFAR telescope

Corresponding author: Jan-Willem Steeb, jwsteeb@gmail.com

Abstract

Radio frequency interference (RFI) is an ever-increasing problem for remote sensing and radio astronomy, with radio telescope arrays especially vulnerable to RFI. Localising the RFI source is the first step to dealing with the culprit system. In this paper, a new localisation algorithm for interferometric arrays with low array beam sidelobes is presented. The algorithm has been adapted to work both in the near-field and far-field (only the direction of arrival can be recovered when the source is in the far-field). In the near-field the computational complexity of the algorithm is linear with search grid size compared to cubic scaling of the state-of-the-art 3D MUSIC method. The new method is as accurate as 3D MUSIC. The trade-off is that the proposed algorithm requires a once-off a priori calculation and storing of weighting matrices. The accuracy of the algorithm is validated using data generated by LOFAR (Low Frequency Array) while a hexacopter was flying around it and broadcasting a continuous-wave signal. For the flight, the mean distance between the differential GPS positions and the corresponding estimated positions of the hexacopter is 2 m at a wavelength of 6.7 m.

1 Introduction

Radio Frequency Interference (RFI) is an important issue in many areas of scientific research, for example in remote sensing and radio astronomy. The ideal solution is to identify the location of the RFI and then remove it. Localisation can either be done using the scientific instrument detecting the RFI or additional equipment. This paper will focus on using radio astronomy interferometric arrays to localise RFI signals. If the RFI source cannot be removed, spatial RFI mitigation methods such as found in [Sardarabadi *et al.*, 2015] and [van der Tol and van der Veen, 2005] can be implemented.

An RFI signal can either be in the near-field or far-field of a sensor array. For sources in the far-field only the direction of arrival information can be recovered. Current source localisation algorithms either make use of brute force methods (such as MUSIC [Balanis and Ioannides, 2007, p. 80-82] where the entire solution space is searched) or exploit the array layout (a common layout is a uniform linear array). Methods that exploit a uniform linear array layout include path following [Starer and Nehorai, 1994], polynomial rooting [Weiss and Friedlander, 1993], weighted linear prediction [Grosicki *et al.*, 2005] and estimation of signal parameters using rotational invariance techniques (ESPRIT) [Yuen and Friedlander, 1998; Challa and Shamsunder, 1995]. In [Huang and Barkat, 1991] and [Hung *et al.*, 1996], an improvement of the MUSIC algorithm is proposed, which replaces searching a dimension with solving the roots of a polynomial. This polynomial arises from calculating a Fourier series which estimates the geometric delay function, but this method introduces an estimation error.

For radio astronomy arrays, brute force methods are computationally expensive due to the high resolution caused by long baselines. Furthermore, to obtain as much information as possible for imaging (optimising the spatial sampling) the array layouts are non-uniform and non-linear. However, radio astronomy interferometric arrays have the advantage that the array beam has low sidelobe levels. Therefore, a novel computationally efficient source localisation algorithm is presented which is designed for irregular interferometric arrays and takes advantage of low array beam sidelobes.

To evaluate the proposed localisation algorithm, 48 of the outer antennas in the Low Band Antenna (LBA) station CS302 of the Low Frequency Array (LOFAR) [van Haarlem *et al.*, 2013] were used. A satellite image of CS302 is given in Figure 1 as well as a plot of the LBA antennas used.

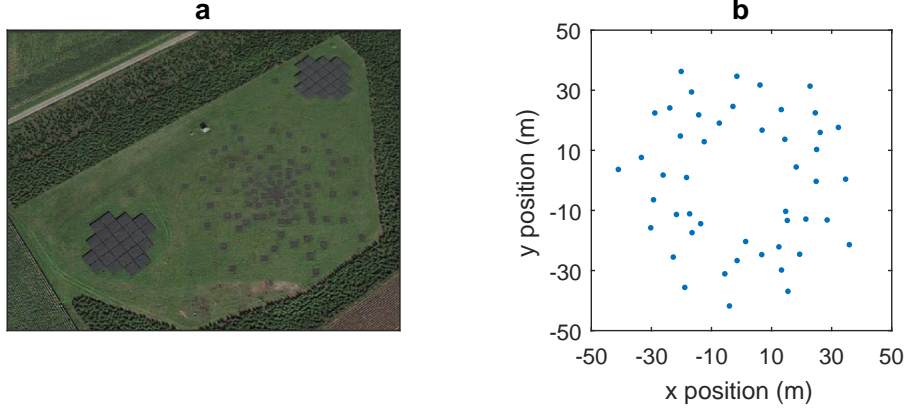


Figure 1. (a) Satellite image of LOFAR station CS302 with a Low Band Antenna (LBA) array in the middle and two High Band Antenna (HBA) arrays flanking it. (b) Array layout of the LOFAR CS302 Low Band Antenna subsystem.

2 Notation

A	Bold upper-case letters are matrices. The jk^{th} element is indicated by \mathbf{A}_{jk} .
a	Bold lower-case letters are column vectors. The j^{th} element is indicated by \mathbf{a}_j .
I	Identity matrix.
\odot	Hadamard product.
$\ \cdot\ $	Euclidean norm of a vector.
$\text{diag}(\cdot)$	Converts a vector into a diagonal matrix.
\angle	Argument of a complex number.
i	Square root of -1.
c	Speed of light.
$\{\cdot\}^H$	Hermitian transpose of a matrix.
$\{\cdot\}^T$	Transpose of a matrix.
$\{\cdot\}^*$	Complex conjugate of a scalar.
$\Re(\cdot)$	Real part of a complex number.
$\mathbb{E}\{\cdot\}$	Expectation operator.

3 Special Functions

In this paper, we use several special functions, that are briefly introduced below. The Exponential integral, denoted by E_1 is given by

$$E_1(z) = \int_z^\infty \frac{e^{-t}}{t} dt = -\gamma - \ln(z) - \sum_{k=1}^{\infty} \frac{(-z)^k}{k k!}, \quad (1)$$

where $\{z \in \mathbb{C} : |\angle z| < \pi\}$ and γ is the Euler-Mascheroni constant. The Bessel function of the first kind, denoted by J_0 is given by

$$J_0(x) = \frac{2}{\pi} \int_0^{\pi/2} \cos(x \sin(\theta)) d\theta = \sum_{k=0}^{\infty} (-1)^k \frac{\left(\frac{1}{4}x^2\right)^k}{(k!)^2}, \quad (2)$$

where $x \in \mathbb{R}$. The Modified Bessel function of the first kind, denoted by I_0 is given by

$$I_0\left(\sqrt{-x^2 - y^2}\right) = \frac{1}{2\pi} \int_0^{2\pi} e^{i(x \sin(\theta) + y \cos(\theta))} d\theta = \sum_{k=0}^{\infty} (-1)^k \frac{\left(\frac{1}{4}(x^2 + y^2)\right)^k}{(k!)^2}, \quad (3)$$

where $x, y \in \mathbb{R}$. The Struve function function, denoted by H_0 is given by

$$H_0(x) = \frac{2}{\pi} \int_0^{\pi/2} \sin(x \sin(\theta)) d\theta = \frac{2}{\pi} \sum_{k=1}^{\infty} \frac{(-1)^k}{[(2k+1)!!]^2} x^{2k+1}, \quad (4)$$

where $x \in \mathbb{R}$.

4 Data Model

We consider the scenario where an array is observing astronomical sources and the measurements are contaminated by a single RFI source. This is later generalised to multiple RFI sources. The assumption is made that the power of the RFI source is considerably higher than the power of the astronomical sources. Therefore, the astronomical sources are omitted from the model. RFI signals are also affected by direction dependent effects such as path loss, polarisation mismatch factor, the gain of the antennas and atmospheric effects. Furthermore, direction independent effects include the receiver electronics, in particular the low noise amplifiers. These effects are usually removed by calibration; however accurate calibration is not possible in the presence of strong RFI. For the j^{th} antenna these effects are contained in the complex gain $g_j(\mathbf{v}_s)$ which is a function of the position vector of the RFI source $\mathbf{v}_s = [x_s, y_s, z_s]^T$.

To keep the model simple the output of the array will only be considered for a single frequency channel and polarisation. The single frequency assumption is reasonable as radio telescopes are usually designed in such a way that their individual frequency channels satisfy the narrowband assumption. Wideband signals, such as DAB broadcasts, will simply be split over multiple channels, for each of which the signal can be treated as a single-frequency signal. If the array consists of N_e elements, then at time t the voltage output can be expressed as [van der Tol and van der Veen, 2005; van der Veen et al., 2004]

$$\mathbf{y}(t) = \mathbf{x}_s(t) + \mathbf{x}_n(t), \quad (5)$$

where $\mathbf{y}(t) = [y_1(t), \dots, y_{N_e}(t)]^T$ is the vector of measured array output signals, $\mathbf{x}_n(t) = [n_1(t), \dots, n_{N_e}(t)]^T$ is the vector of instrumental noise for each antenna and $\mathbf{x}_s(t)$ is the vector describing the RFI signal, which experiences a delay for each antenna. This term is described in detail below.

For the j^{th} antenna, τ_j is the delay between the source location and the array element. If the delayed signal $s(t - \tau_j)$ is to be used in the formulation of a covariance matrix model (see equation (10)), it can be approximated by $s(t - \tau_j) \approx s(t) e^{-i2\pi\nu\tau_j}$, where ν is the centre frequency of the channel. This can be done, since only the delay differences between antennas $\tau_{jk} = \tau_j - \tau_k$ are of importance in the covariance matrix model (see equation (10) in conjunction with equation (6)). This approximation is possible if the signal is sufficiently narrowband, that is $2\pi\Delta\nu\tau_{\max} \ll 1$ [Zatman, 1998], where $\Delta\nu$ is the signal's bandwidth and $\tau_{\max} = \tau_j - \tau_k$ such that the j^{th} and k^{th} antenna have the longest baseline (distance between antennas) and a straight line can be traced through the source and the two antennas. The phase delays of the source can be stacked into a vector that is called the geometric delay vector

$$\mathbf{a}(\mathbf{v}_s) = \begin{bmatrix} e^{-i2\pi\nu\tau_1} \\ \vdots \\ e^{-i2\pi\nu\tau_{N_e}} \end{bmatrix}. \quad (6)$$

When the RFI source is in the near-field, the j^{th} delay is given by $\tau_j = \|\mathbf{v}_s - \mathbf{v}_j\|/c$, where $\mathbf{v}_j = [x_j, y_j, z_j]$ is the position vector of the antenna. For the far-field case, the j^{th} delay is given by $\tau_j = -(\mathbf{v}_{s,\text{ff}}^T \mathbf{v}_j)/c$, where $\mathbf{v}_{s,\text{ff}}^T = [\sin(\theta_s) \cos(\phi_s), \sin(\theta_s) \sin(\phi_s), \cos(\theta_s)]^T$ is a direction vector. The angles θ_s and ϕ_s are respectively the polar and azimuthal

angles of the RFI source. The model in equation (5) can be rewritten, using $\mathbf{a}(\mathbf{v}_s)$ and $\mathbf{g}(\mathbf{v}_s)$, as

$$\mathbf{y}(t) = \mathbf{a}(\mathbf{v}_s) \odot \mathbf{g}(\mathbf{v}_s) s(t) + \mathbf{x}_n(t), \quad (7)$$

where $\mathbf{g}(\mathbf{v}_s) = [g_1(\mathbf{v}_s), \dots, g_{N_e}(\mathbf{v}_s)]^T$ is a vector that contains the complex gain for each antenna. To create images, radio interferometric arrays use the covariance matrix of the signals

$$\mathbf{R} = \mathbb{E}\{\mathbf{y}(t)\mathbf{y}^H(t)\}. \quad (8)$$

This matrix can only be estimated by assuming that all signals are stationary for short time periods, that is

$$\hat{\mathbf{R}} = \frac{1}{N_t} \sum_{l=1}^{N_t} \mathbf{y}(lT_s)\mathbf{y}^H(lT_s), \quad (9)$$

where $\hat{\mathbf{R}}$ is the estimated covariance matrix, N_t is the number of samples for which the signals are stationary and T_s is the sample time.

The covariance matrix and its estimate are Hermitian (complex symmetric) where the kj^{th} element of the matrix is the correlation of the k^{th} and j^{th} antenna and the kj^{th} element and jk^{th} element are complex conjugates of each other.

Independence is assumed between the RFI source and the noise. Therefore, when substituting equation (7) into equation (8) the expectation of any non-self multiplication term is zero and consequently the substitution yields

$$\begin{aligned} \mathbf{R} &= \mathbf{R}_s + \mathbf{R}_n \\ &= (\mathbf{a}(\mathbf{v}_s) \odot \mathbf{g}(\mathbf{v}_s)) \sigma_s^2 (\mathbf{g}(\mathbf{v}_s) \odot \mathbf{a}(\mathbf{v}_s))^H + \mathbf{R}_n, \end{aligned} \quad (10)$$

where $\sigma_s^2 = \mathbb{E}\{s(t)s^*(t)\}$ is the power of the RFI signal, since the signal has zero mean. If N_s RFI signals are present, the covariance matrix is the sum of the covariance matrices ($\mathbf{R}_{s,j}$) for each signal

$$\begin{aligned} \mathbf{R} &= \sum_{j=1}^{N_s} \mathbf{R}_{s,j} + \mathbf{R}_n \\ &= \mathbf{R}_\Sigma + \mathbf{R}_n \\ &= (\mathbf{A}(\mathbf{V}_s) \odot \mathbf{G}(\mathbf{V}_s)) \mathbf{S} (\mathbf{G}(\mathbf{V}_s) \odot \mathbf{A}(\mathbf{V}_s))^H + \mathbf{R}_n, \end{aligned} \quad (11)$$

because all the operators used are linear, where $\mathbf{A}(\mathbf{V}_s) = [\mathbf{a}(\mathbf{v}_{s,1}), \dots, \mathbf{a}(\mathbf{v}_{s,N_s})]$, $\mathbf{G}(\mathbf{V}_s) = [\mathbf{g}(\mathbf{v}_{s,1}), \dots, \mathbf{g}(\mathbf{v}_{s,N_s})]$, $\mathbf{V}_s = [\mathbf{v}_{s,1}, \dots, \mathbf{v}_{s,N_s}]$ and $\mathbf{S} = \text{diag}([\sigma_{s,1}^2, \dots, \sigma_{s,N_s}^2])$.

A classical delay beamformer (CDB) $\mathbf{b}_{\text{CDB}}(\mathbf{v}) = (\mathbf{a}^H(\mathbf{v})\mathbf{a}(\mathbf{v}))^{-1}\mathbf{a}^H(\mathbf{v})$, can be used to create a dirty image [Thompson et al., 2004, p. 427-430] from the covariance matrix by calculating for every voxel [Balanis and Ioannides, 2007, p. 78]

$$\begin{aligned} J(\mathbf{v}) &= \mathbb{E}\{\mathbf{b}_{\text{CDB}}(\mathbf{v})\mathbf{y}(t)(\mathbf{b}_{\text{CDB}}(\mathbf{v})\mathbf{y}(t))^H\} \\ &= \mathbf{b}_{\text{CDB}}(\mathbf{v})\mathbf{R}\mathbf{b}_{\text{CDB}}^H(\mathbf{v}) \\ &= \frac{1}{N_e^2} \mathbf{a}^H(\mathbf{v})\mathbf{R}\mathbf{a}(\mathbf{v}). \end{aligned} \quad (12)$$

A peak in this image indicates the position of a source.

5 Proposed Source Localisation Algorithm

Before the localisation algorithm is applied, the RFI must be detected, for which methods described in [van der Tol and van der Veen, 2005; van der Veen et al., 2004] can be used. The proposed localisation algorithm consists of three stages. The first is preprocessing, which attempts to remove instrumental noise signals and isolate individual RFI sources. This is followed by the integrating-out-variables method which exploits the low sidelobes and which produces a reasonable estimate. This estimate is then used as the initial guess for a fast converging iterative method in the final step.

5.1 Stage 1: Preprocessing

The objective of the preprocessing step is to reduce the effect of the instrumental noise signals and isolate individual RFI sources. It is assumed that the power of the RFI signals is above the noise. As the instrumental noise signal may be different for different antennas, the noise powers in \mathbf{R}_n will differ. However, the assumption is made that the instrumental noise signals of the antennas are independent, therefore \mathbf{R}_n is a diagonal matrix.

To remove the effect of \mathbf{R}_n on \mathbf{R} a statistical method such as complex factor analysis [Sardarabadi, 2016, p. 31-60] can be used, which decomposes the $N_e \times N_e$ covariance matrix into $\mathbf{R} = \mathbf{Z}\mathbf{Z}^H + \mathbf{D}$, where \mathbf{Z} is an $N_e \times N_f$ matrix and \mathbf{D} is a diagonal $N_e \times N_e$ matrix. If the method is applied successfully, $\mathbf{D} \approx \mathbf{R}_n$ and therefore $\mathbf{Z}\mathbf{Z}^H \approx \mathbf{R}_\Sigma$ (see equation (11)). If the columns of $\mathbf{A}(\mathbf{V}_s) \odot \mathbf{G}(\mathbf{V}_s)$ are linearly independent and $N_s < N_e$, then $N_f = N_s$. For the method to converge, an upper limit on the number of factors N_f , namely $N_f < (N_e - \sqrt{N_e})$, is imposed [van der Veen et al., 2004]. The columns of \mathbf{Z} are now used to construct a set of new covariance matrices

$$\begin{aligned} \mathbf{R}_{f,1} &= \mathbf{Z}(:,1)\mathbf{Z}^H(:,1), \\ &\vdots \\ \mathbf{R}_{f,N_s} &= \mathbf{Z}(:,N_s)\mathbf{Z}^H(:,N_s). \end{aligned}$$

Consequently, the sources are separated in these covariance matrices and in the ideal case, where the columns of $\mathbf{A}(\mathbf{V}_s) \odot \mathbf{G}(\mathbf{V}_s)$ are orthogonal, each $\mathbf{R}_{f,j}$ will match with an $\mathbf{R}_{s,j}$. In most radio astronomy data sets, a single snapshot covariance matrix is affected by only one or two RFI sources and, even though the columns of $\mathbf{A}(\mathbf{V}_s) \odot \mathbf{G}(\mathbf{V}_s)$ may not be orthogonal, the separation is sufficient for each $\mathbf{R}_{f,j}$ to contain the majority of one source's power.

The largest gain differences between the near-field signal received by multiple elements, are caused by path loss differences which only affect the amplitudes of the gains. This effect can be removed by considering only the phase information.

5.2 Stage 2: Integrating-out-variables

Let the matrix $\mathbf{U} = e^{i\angle\mathbf{R}_{f,j}}$, where $e^{i\angle\mathbf{R}_{f,j}}$ is a result from the preprocessing step. Since \mathbf{U} is Hermitian with no amplitude information, all the information is contained in the top (or bottom) triangular part of \mathbf{U} . There is a total of $N_b = (N_e^2 - N_e)/2$ elements in both the triangular parts, which is equal to the number of antenna combinations (also called baselines). By stacking the transposed rows of the top triangular part of \mathbf{U} , an $N_b \times 1$ vector $\boldsymbol{\beta}$ is created. If the top triangular part of \mathbf{U} is used, then the relationship between the p^{th} element of $\boldsymbol{\beta}$ and the jk^{th} element of \mathbf{U} is $p = (j-1)N_e - 0.5(j^2 + j) + k$, where $j \in \{1, \dots, N_e - 1\}$ and $k \in \{j+1, \dots, N_e\}$.

The classical delay beamformer spectrum (see equation (12)) for \mathbf{U} can then be rewritten as a sum (the dependency on \mathbf{v}_s will be omitted to make the notation more concise)

$$J = \frac{1}{N_e} + \frac{2}{N_e^2} \sum_{p=1}^{N_b} \Re[\boldsymbol{\beta}_p e^{-i\zeta_p}], \quad (13)$$

where vector $\boldsymbol{\zeta}$ contains the stacked (similar to $\boldsymbol{\beta}$) angle differences $\gamma_j - \gamma_k$ and

$$\begin{aligned} \gamma_j &= \frac{-2\pi\nu}{c} \|\mathbf{v} - \mathbf{v}_j\| \\ &= \frac{-2\pi\nu}{c} \sqrt{r^2 - 2r(\sin(\theta)\cos(\phi)x_j + \sin(\theta)\sin(\phi)y_j + \cos(\theta)z_j) + r_j^2}. \end{aligned} \quad (14)$$

The coordinates of the voxel have been written in spherical coordinates (r, θ, ϕ) and (x_j, y_j, z_j) is the position of the j^{th} antenna. The traditional method to find the location of the source requires that a beamformer must be constructed for every voxel in the near-field, where the number of voxels is dependent on the resolution as well as the size of the near-field. This problem therefore has computational complexity $\mathcal{O}(N_r \times N_\theta \times N_\phi)$, where N_r , N_θ , N_ϕ are, respectively, the number of r , θ and ϕ values.

To reduce the computational complexity of finding a source location from cubic to linear, the proposed method integrates out variables and then only varies one variable to find the peak. The complex exponential function in equation (13) can not be analytically integrated. Therefore, the integration is done numerically once a priori and is stored (the trade off is therefore that the storage requirement increases). The algorithm notation is: $\boldsymbol{\phi}$ is an $N_\phi \times 1$ vector of ϕ values, $\boldsymbol{\theta}$ is an $N_\theta \times 1$ vector of θ values, \mathbf{r} is an $N_r \times 1$ vector of r values, r_a is the minimum radius wherein all the array elements lie and $r_{\text{nf}} = b_{\text{max}}^2 \nu_0 / c$ is the radius at which the transition from radiating near-field to far-field starts [Thompson *et al.*, 2004, p. 601] and b_{max} is the length of the longest baseline. Two weighting matrices are calculated a priori:

1. First weighting matrix:

$$\mathbf{W}_1(p, n) = \int_0^{\pi/2} \int_{r_a}^{r_{\text{nf}}} e^{-i\zeta_p(\phi_n)} dr d\theta, \quad (15)$$

with dimension $N_b \times N_\phi$ and $\phi_n \in [-\pi, \pi]$. The θ integral is over 0 to $\pi/2$, because only one hemisphere needs to be considered for an Earth based array.

2. Second weighting matrix:

$$\mathbf{W}_2(p, m, n) = \int_{r_a}^{r_{\text{nf}}} e^{-i\zeta_p(\theta_m, \phi_n)} dr, \quad (16)$$

with dimension $N_b \times N_\theta \times N_\phi$, $\phi_n \in [-\pi, \pi]$ and $\theta_m \in [0, \pi/2]$.

The weighting matrices \mathbf{W}_1 and \mathbf{W}_2 are calculated only once for a given array and frequency. The steps of the algorithm are:

1. Calculate

$$f_1(\boldsymbol{\phi}(n)) = \sum_{p=1}^{N_b} \Re [\boldsymbol{\beta}_p \mathbf{W}_1(p, n)], \quad (17)$$

for $n = 1, \dots, N_\phi$. Find the peak of f_1 and the corresponding index n_ϕ of $\boldsymbol{\phi}$.

2. Use index n_ϕ to fix $\boldsymbol{\phi}$ and find the peak of

$$f_2(\boldsymbol{\theta}(m)) = \sum_{p=1}^{N_b} \Re [\boldsymbol{\beta}_p \mathbf{W}_2(p, m, n_\phi)], \quad (18)$$

for $m = 1, \dots, N_\theta$. Find the peak of f_2 and the corresponding index m_θ of $\boldsymbol{\theta}$.

3. Use n_ϕ and m_θ to fix $\boldsymbol{\phi}$ and $\boldsymbol{\theta}$, respectively, and use normalised one dimensional classical delay beamforming imaging (see equation (12)) to obtain a value for r . If the recovered value is not close to 1, return to the first step and choose the next highest peak (and repeat this N_i times until the threshold is met or there are no more peaks).

The position obtained is just an estimate and the accuracy is dependent on how low the sidelobe levels are. This method only needs to search an $(N_r + N_\theta + N_\phi)$ array N_i times, while 3D MUSIC must search a 3-dimensional grid $(N_r \times N_\theta \times N_\phi)$. In our simulations, we found that N_i is almost always equal to 1.

5.2.1 Stage 2: Storage Requirement Reduction

For each iteration of stage 2 of the algorithm, all values in matrix \mathbf{W}_1 are used, however only an N_ϕ^{th} part of \mathbf{W}_2 is used, since n_ϕ is fixed. The memory requirement can be reduced by calculating the required weights on the fly. For the jk^{th} baseline and fixed values for θ and ϕ the required integral is

$$\mathbf{W}_2(p, m, n_\phi) = \int_{r_a}^{r_{\text{nf}}} e^{-i[\gamma_j(r) - \gamma_k(r)]} dr. \quad (19)$$

This integral cannot be analytically solved and solving it numerically is computationally expensive. Defining $d_j = -2(\sin(\theta) \cos(\phi)x_j + \sin(\theta) \sin(\phi)y_j + \cos(\theta)z_j)$ and applying the Taylor expansion to equation (14) yields

$$\begin{aligned} \gamma_j &= \frac{-2\pi\nu}{c} \sqrt{r^2 + d_j r + r_j^2} \\ &= \frac{-2\pi\nu}{c} r \sqrt{1 + \frac{d_j r + r_j^2}{r^2}} \\ &\approx \frac{-2\pi\nu}{c} \left[r + \frac{d_j}{2} + \frac{4r_j^2 - d_j^2}{8r} \right], \end{aligned} \quad (20)$$

with the assumption that $r^2 > d_j r + r_j^2$ (which is valid since the integral starts outside the array). The argument of the complex exponential is then approximated by

$$\begin{aligned} \gamma_j - \gamma_k &\approx \frac{-2\pi\nu}{c} \left[\frac{d_j - d_k}{2} + \frac{4(r_j^2 - r_k^2) - (d_j^2 - d_k^2)}{8r} \right] \\ &= a + \frac{b}{r}, \end{aligned} \quad (21)$$

where

$$\begin{aligned} a &= -\pi\nu c^{-1} [d_j - d_k], \\ b &= -\frac{1}{4} \pi\nu c^{-1} [4(r_j^2 - r_k^2) - (d_j^2 - d_k^2)]. \end{aligned}$$

Using the approximation in equation (21) the integral in equation (19) can be solved by using the exponential integral function

$$\begin{aligned} \mathbf{W}_2(p, n, m) &\approx \widetilde{\mathbf{W}}_2(p, n, m) = \int_{r_a}^{r_{\text{nf}}} e^{-i[a+b/r]} dr \\ &= e^{-ia} \left[ib \operatorname{E}_1\left(\frac{ib}{r_a}\right) - ib \operatorname{E}_1\left(\frac{ib}{r_{\text{nf}}}\right) - r_a e^{-ib/r_a} + r_{\text{nf}} e^{-ib/r_{\text{nf}}} \right] \end{aligned} \quad (22)$$

where $|\angle \frac{ib}{r_a}| = |\angle \frac{ib}{r_{\text{nf}}}| = \frac{\pi}{2}$, because both arguments are only complex. A comparison of the compute time of Matlab's global adaptive quadrature method and equation (22) showed a 7 times speed-up, at a frequency of 44.5 MHz using the LOFAR station's CS302 layout (a desktop computer with an Intel Core i5-2500k chip was used). To measure the accuracy of the approximation the mean absolute percentage error is used

$$\mathbf{M}(n, m) = 100 \sum_{p=1}^{N_b} \left| \frac{\mathbf{W}_2(p, n, m) - \widetilde{\mathbf{W}}_2(p, n, m)}{N_b \mathbf{W}_2(p, n, m)} \right|. \quad (23)$$

In Figure 2 a plot of \mathbf{M} is given with a maximum mean absolute percentage error of 6 % which occurs at approximately $\theta = \pi/4$.

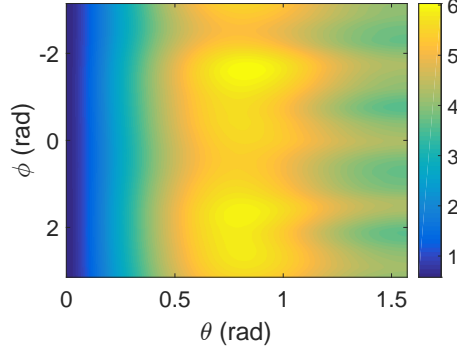


Figure 2. Plot of the mean absolute percentage error of $\widetilde{\mathbf{W}}_2$ as a function of θ and ϕ (see equation (23)). LOFAR station's CS302 layout was used at a frequency of 44.5 MHz.

5.2.2 Stage 2: Far-field Approach

For the far-field case the classical delay beamformer (see equation (13)) is also used, however it is a function of $\mathbf{v}_{s,\text{ff}}$ and equation (14) is now given by

$$\begin{aligned}\gamma_j &= \frac{2\pi\nu}{c} \mathbf{v}_{s,\text{ff}}^T \mathbf{v}_j \\ &= \frac{2\pi\nu}{c} (\sin(\theta) \cos(\phi) x_j + \sin(\theta) \sin(\phi) y_j + \cos(\theta) z_j).\end{aligned}\quad (24)$$

Since equation (24) is a function of (θ, ϕ) , only θ has to be integrated out to generate a weighting matrix. The complex exponential that is integrated can be solved in terms of special functions if $\theta \in [0, 2\pi]$ (instead of $\theta \in [0, \pi/2]$) as follows

$$\begin{aligned}\mathbf{W}_{1,\text{ff}}(p, n) &= \int_0^{2\pi} e^{-i\zeta_p(\phi_n)} d\theta = \int_0^{2\pi} e^{-i[\gamma_j(\phi_n) - \gamma_k(\phi_n)]} d\theta \\ &= \int_0^{2\pi} e^{-i[a \sin(\theta) + b \cos(\theta)]} d\theta \\ &= 2\pi I_0 \left(\sqrt{-a^2 - b^2} \right),\end{aligned}\quad (25)$$

where

$$\begin{aligned}a &= i2\pi\nu c^{-1} (\cos(\phi_n)(x_j - x_k) + \sin(\phi_n)(y_j - y_k)), \\ b &= i2\pi\nu c^{-1} (z_j - z_k).\end{aligned}$$

Integrating over 2π will cause a mirror image when plotting $f_{1,\text{ff}}(\phi(k))$ as given by equation (27). Therefore, each peak will have to be investigated. In the special case that the array is planar, that is $z_j = 0$, it is possible to do the integral over $\pi/2$

$$\begin{aligned}\mathbf{W}_{1,\text{ff}}(p, n) &= \int_0^{\pi/2} e^{-ia \sin(\theta)} d\theta \\ &= \frac{\pi}{2} [J_0(a) + iH_0(a)].\end{aligned}\quad (26)$$

The weighting matrix $\mathbf{W}_{1,\text{ff}}$ is calculated only once for a given array and frequency. The steps of the algorithm are:

1. Calculate

$$f_{1,\text{ff}}(\phi(n)) = \sum_{p=1}^{N_b} \Re [\beta_p \mathbf{W}_{1,\text{ff}}(p, n)],\quad (27)$$

- for $n = 1, \dots, N_\phi$. Find the peak of $f_{1,\text{ff}}$ and the corresponding index n_ϕ of ϕ .
2. Use n_ϕ to fix ϕ and use normalised one dimensional near-field classical delay beamforming imaging (see equation (12)) to obtain a value for θ . If the recovered value is not close to 1, return to the first step and choose the next highest peak (and repeat this N_i times until the threshold is met or there are no more peaks).

This method only needs to search an $(N_\theta + N_\phi)$ array N_i times, while 2D MUSIC must search a 2-dimensional grid $(N_\theta \times N_\phi)$.

5.3 Stage 3: Minimum Error Convergence

The proposed convergence algorithm uses the same concepts as those found in [Wijnholds et al., 2016], which are used for antenna position calibration. The core idea is that $\mathbf{a}(\mathbf{v})\mathbf{a}^H(\mathbf{v})$ can be linearised if the error of the estimate of \mathbf{v}_s is sufficiently small. If it is assumed that the effect of $\mathbf{G}(\mathbf{V}_s)$ can be discounted and only one source is present, then

$$\angle \mathbf{U}_{jk} = \frac{-2\pi\nu}{c} (\|\mathbf{v}_s - \mathbf{v}_j\| - \|\mathbf{v}_s - \mathbf{v}_k\|) + 2\pi m_{jk}, \quad (28)$$

where m_{jk} is an integer that represents the phase ambiguity. Let $\boldsymbol{\delta}_j = \mathbf{v}_s^o - \mathbf{v}_j$, where \mathbf{v}_s^o is an estimate of the RFI position. Assume that the error $\boldsymbol{\epsilon} = \mathbf{v}_s^o - \mathbf{v}_s$ is small, then the Taylor expansion yields

$$\begin{aligned} \|\mathbf{v}_s - \mathbf{v}_j\| = \|\boldsymbol{\delta}_j - \boldsymbol{\epsilon}\| &= \sqrt{\|\boldsymbol{\delta}_j\|^2 + \|\boldsymbol{\epsilon}\|^2 - 2\boldsymbol{\delta}_j^T \boldsymbol{\epsilon}} \\ &\approx \sqrt{\|\boldsymbol{\delta}_j\|^2 - 2\boldsymbol{\delta}_j^T \boldsymbol{\epsilon}} \\ &= \|\boldsymbol{\delta}_j\| \sqrt{1 - \frac{2\boldsymbol{\delta}_j^T \boldsymbol{\epsilon}}{\|\boldsymbol{\delta}_j\|^2}} \\ &\approx \|\boldsymbol{\delta}_j\| - \frac{\boldsymbol{\delta}_j^T \boldsymbol{\epsilon}}{\|\boldsymbol{\delta}_j\|}. \end{aligned} \quad (29)$$

Substituting equation (29) into equation (28) yields a linear equation in terms of $\boldsymbol{\epsilon}$

$$\angle \mathbf{U}_{jk} \approx \frac{-2\pi\nu}{c} \left[\|\boldsymbol{\delta}_j\| - \|\boldsymbol{\delta}_k\| + \left(\frac{-\boldsymbol{\delta}_j}{\|\boldsymbol{\delta}_j\|} + \frac{\boldsymbol{\delta}_k}{\|\boldsymbol{\delta}_k\|} \right)^T \boldsymbol{\epsilon} \right] + 2\pi m_{jk}. \quad (30)$$

Using the approximation in equation (30), define

$$\mathbf{B}_{jk} = \left(\frac{-\boldsymbol{\delta}_j}{\|\boldsymbol{\delta}_j\|} + \frac{\boldsymbol{\delta}_k}{\|\boldsymbol{\delta}_k\|} \right)^T \boldsymbol{\epsilon} \approx \angle \left[\mathbf{U}_{jk} e^{\frac{i2\pi\nu}{c} (\|\boldsymbol{\delta}_j\| - \|\boldsymbol{\delta}_k\|)} \right] \frac{-c}{2\pi\nu}, \quad (31)$$

which only holds if $\boldsymbol{\epsilon}$ is sufficiently small so that the phase ambiguity m_{jk} is zero. By stacking the transposed rows of the top triangular part of \mathbf{B} , an $N_b \times 1$ vector can be created

$$\mathbf{b} = \mathbf{M}\boldsymbol{\epsilon}, \quad (32)$$

where \mathbf{M} is an $N_b \times 3$ matrix consisting of the stacked $\left(\frac{-\boldsymbol{\delta}_j}{\|\boldsymbol{\delta}_j\|} + \frac{\boldsymbol{\delta}_k}{\|\boldsymbol{\delta}_k\|} \right)$ vectors. Equation (32) is used to define the least squares (LS) problem $\hat{\boldsymbol{\epsilon}} = \arg \min_{\boldsymbol{\epsilon}} \|\mathbf{b} - \mathbf{M}\boldsymbol{\epsilon}\|^2$. The optimal solution in an LS sense is

$$\hat{\boldsymbol{\epsilon}} = (\mathbf{M}^H \mathbf{M})^{-1} \mathbf{M}^H \mathbf{b}. \quad (33)$$

When equation (33) is used to calculate $\hat{\boldsymbol{\epsilon}}$ iteratively and the estimate $\mathbf{v}_s^o := \mathbf{v}_s^o - \hat{\boldsymbol{\epsilon}}$ is updated, the estimate \mathbf{v}_s^o converges to \mathbf{v}_s if the initial estimate of \mathbf{v}_s is within the main lobe of the beamformer.

5.3.1 Stage 3: *z*-Direction search correction step

The minimum convergence algorithm may not always converge correctly if the source lies close to the horizon for a planar array (due to the low resolution). Convergence can be improved by doing one dimensional classical delay beamforming imaging (see equation (12)) in the *z*-direction, after the first attempt of the minimum convergence algorithm. The new estimate of *z* is then used to complete a second run of the minimum convergence algorithm.

5.3.2 Stage 3: *Far-field Approach*

When the source is in the far field a Taylor expansion is not necessary (see equation (29)), because the model for the phase is already linear

$$\begin{aligned}\angle \mathbf{U}_{jk} &= \frac{2\pi\nu}{c}(\mathbf{v}_j - \mathbf{v}_k)^T \mathbf{v}_{s,\text{ff}} + 2\pi m_{jk} \\ &= \frac{2\pi\nu}{c}(\mathbf{v}_j - \mathbf{v}_k)^T (\mathbf{v}_{s,\text{ff}}^o - \boldsymbol{\epsilon}) + 2\pi m_{jk},\end{aligned}\quad (34)$$

where $\mathbf{v}_{s,\text{ff}}^o$ is the estimate of the direction vector of the RFI and $\boldsymbol{\epsilon} = \mathbf{v}_{s,\text{ff}}^o - \mathbf{v}_{s,\text{ff}}$. Using the approximation in equation (34), define

$$\begin{aligned}\mathbf{B}_{jk} &= \angle \left[\mathbf{U}_{jk} e^{\frac{-i2\pi\nu}{c}(\mathbf{v}_j - \mathbf{v}_k)^T \mathbf{v}_{s,\text{ff}}^o} \right] \frac{c}{2\pi\nu} \\ &= (\mathbf{v}_j - \mathbf{v}_k)^T \boldsymbol{\epsilon}.\end{aligned}\quad (35)$$

The least squares method outlined in equations (32) and (33) can be used to improve the estimate $\mathbf{v}_{s,\text{ff}}^o$.

6 High Level Overview of Proposed Algorithm

Figure 3 contains a UML activity diagram of the algorithm used to distinguish between far-field and near-field sources. Initially it is assumed that no previous RFI source was found (`prev_found = 0`) and that the first source to be detected lies within the far-field (`far_field = 1`). The initial far-field assumption is made because the far-field version of the algorithm is computationally less expensive. If the far-field algorithm fails to converge (`[conv == 0]`) the near-field algorithm is attempted. It is also possible that the far-field algorithm converges for a near-field source, consequently a one dimensional classical delay beamforming imaging (1D Search *r*) is done to check if the radial distance is larger than r_{nf} . If RFI was previously localised, then just the minimum error convergence (MEC) stage is attempted using the previously found RFI coordinates as an initial estimate, thereby reducing computational cost and enabling the algorithm to track moving RFI sources. For the hexacopter data (see Section 9), using the tracking feature reduced the total computational time from 556 s to 5.2 s.

7 Simulation in the Near-field

To evaluate the proposed algorithm, a simulation was done using the layout of the 48 coplanar antennas from the LOFAR CS302 station Low Band Antenna (LBA) subsystem (see Figure 1b) at a frequency of 44.5 MHz. A uniform distribution was used to generate 5000 random source positions which lie outside the aforementioned array, but within the array near-field. From the positions, covariance matrices were generated where the complex gains were set to $\mathbf{g}(\mathbf{V}_s) = \mathbf{1}$ and the algorithm was applied to each one. The case where the complex gains are not unity is discussed in Section 9.

For only 1.46 % of the covariance matrices did the integrating-out-variables method have to iterate more than once. The reason for this is that, for some directions,

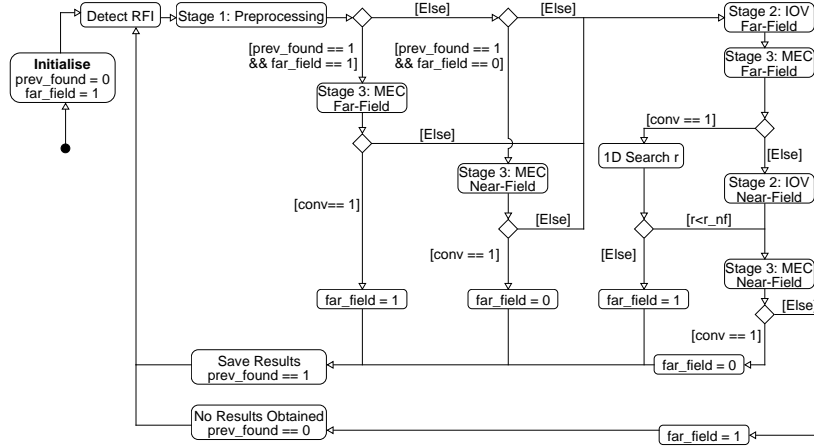


Figure 3. UML activity diagram of the proposed algorithm.

the beamformer has sidelobes that create peaks in f_1 that are greater than the peak at the source's angle ϕ_s . In Figure 4 plots of the number of peaks of f_1 that had to be tested as a function of the spherical coordinates of the source, is given. These plots show that the region most susceptible to distortion is the reactive near-field, which transitions to the radiating near-field at about 200 m from the array.

For 98 % of the runs, the algorithm took less than 0.2 s (the mean of all runs is 0.18 s and the maximum 1.5 s), see the histogram in Figure 5a. The relative frequency histogram in Figure 5b shows that for 98 % of the runs the convergence algorithm took 4 or 5 iterations.

To measure the accuracy of the algorithm, the Euclidean distance (now called the distance error) between the position of each source (\mathbf{v}_s) and its corresponding estimated position ($\tilde{\mathbf{v}}_s$) was calculated. For the i^{th} run, the Euclidean distance is then $\mathbf{d}_i = \|\mathbf{v}_{s,i} - \tilde{\mathbf{v}}_{s,i}\|$. The mean distance error and mean absolute deviation for the simulation are given, respectively, by

$$\text{MDE} = \sum_i^{N_r} \frac{\mathbf{d}_i}{N_r}, \quad (36)$$

$$\text{MAD} = \sum_i^{N_r} \frac{|\mathbf{d}_i - \text{mean}(\mathbf{d})|}{N_r}, \quad (37)$$

where N_r is the number runs. The integrating-out-variables stage yielded a mean distance error of 7.57 m with a mean absolute deviation of 6.08 m (see Figure 5c). After the convergence step, without the z -direction search correction step, only 0.92% of the distance errors are non-zero, see Figure 5d. These outliers all lie within 0.04 rad of the horizon, lie further than 170 m from the array centre and the error appears in the z -direction (the direction orthogonal to the plane that the array lies in). This occurs because the array is planar and therefore it is more difficult to resolve the z coordinate for sources further away from the array and closer to the horizon. After the convergence stage, with a z -direction search correction step (see Section 5.3.1), the mean as well as the spread of the distance errors are reduced to 0 (this is only possible because there is no noise or calibration errors in the simulated system).

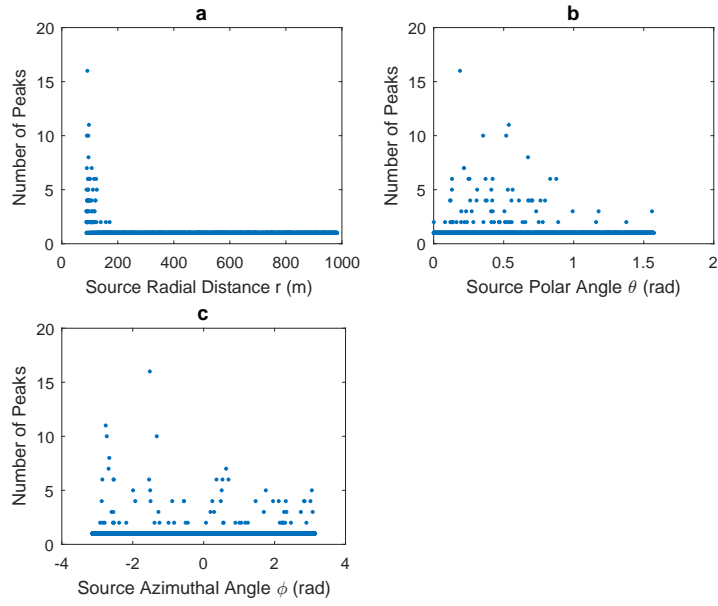


Figure 4. The number of peaks of f_1 which had to be tested before the threshold condition was met, (a) as function of the radial distance of the source, (b) as a function of the polar angle of the source, (c) as a function of the azimuthal angle of the source.

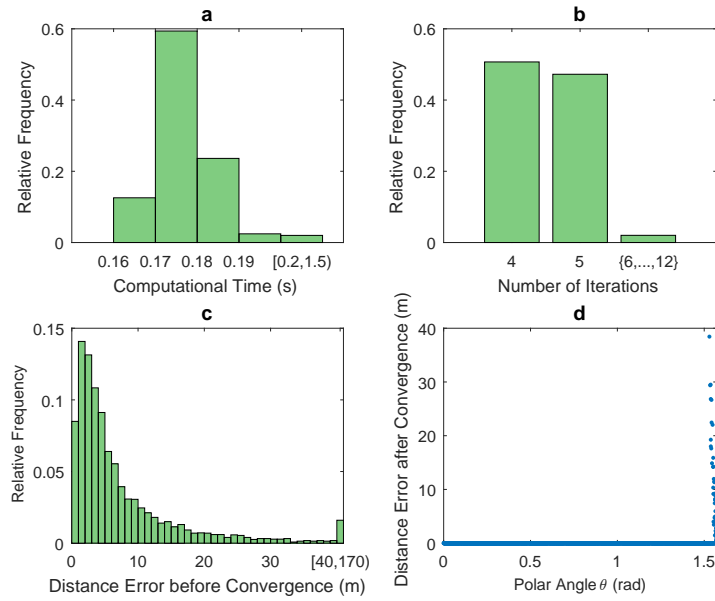


Figure 5. (a) Relative frequency histogram of the computational time for 5000 runs. (b) Relative frequency histogram of the number of iterations required by the convergence stage for 5000 runs. (c) Relative frequency histogram of the distance error before the convergence stage for 5000 runs. (d) Distance error after the convergence stage as a function of polar angle θ for 5000 runs without a z direction search correction step (see Section 5.3.1).

8 Calibration Error Performance

To test the effect of direction independent calibration errors on the algorithm, a normal distribution was used to generate phases to calculate \mathbf{g} (see equation (10)). The distribution has mean 0 and the standard deviation was varied between 0 and $\pi/3$ radians. At the final standard deviation of $\pi/3$, 99.73 % of the values lie within a π -rad band around the mean. For each standard deviation a thousand realisations for each antenna were calculated. In Figure 6a two plots are given for the averaged results of the thousand realisations. The first shows that the averaged normalised CDB spectrum deteriorates as a function of standard deviation, whilst the second plot shows that the mean distance error increases linearly. The threshold of a successful estimation was set to a mean distance error of 135 m (this is the mean distance error value where the averaged normalised CDB spectrum is at half power and the standard deviation is the same). In Figure 6b, the proportion or simulated probability of an incorrect estimation is approximately zero for standard deviation in $[0, \pi/12]$. However, for standard deviation in $(\pi/12, \pi/3]$ the simulated probability increases approximately linearly from 0 to 0.43.

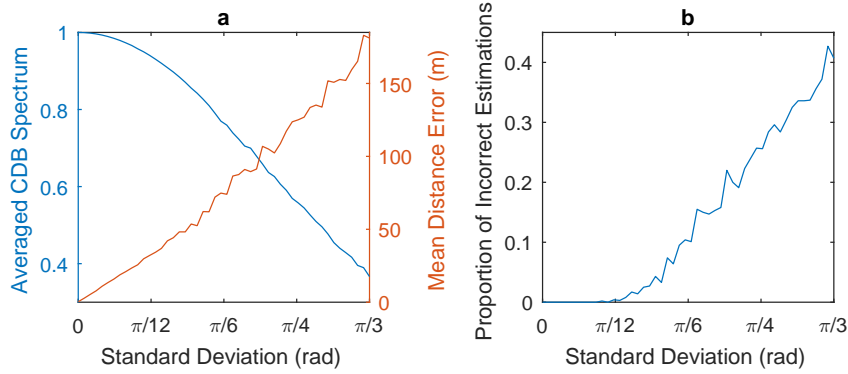


Figure 6. (a) Plots of averaged normalised CDB spectrum and MDE, respectively, as a function of standard deviation. (b) Simulated probability for incorrect estimation of RFI location plotted against standard deviation.

9 Testing of the Algorithm on Data from a LOFAR Station

The algorithm is further validated by using data generated by 48 low band antennas from LOFAR station CS302 when a hexacopter was flown around the array broadcasting continuous-wave signals with different frequencies [Bollini *et al.*, 2017]. The time series data of the sub-band with centre frequency 44.5 MHz was selected and every 0.2 s the data was correlated for 20 ms (this short correlation time was chosen so that the hexacopter could be assumed stationary). Furthermore, the hexacopter recorded its location using differential GPS (accuracy ~ 1 cm) and this information was used to calculate the distance errors (GPS data was recorded every 0.2 s). The main difference between the simulation and real data is that the complex gains $\mathbf{G}(\mathbf{V}_s)$ are no longer 1, since the array is not calibrated. After the convergence stage the mean distance error reduced from 4 m to 2 m (with mean absolute deviation of 1.16 m) which is less than the wavelength of 6.7 m, see Figure 7a. The mean distance error for the hexacopter data, before the convergence stage, is smaller than that of the simulation. This is due to the simulation containing sources with locations that are more challenging for stage 2 to resolve. However, after the convergence stage the simulation showed no error in the estimated location.

The distance error plot in Figure 7a forms an oscillating curve and has a pattern similar to the plot of the radial distance that the hexacopter is from the array. This is due to the effect of antenna gain errors on the covariance matrix, which increases the distance error as the radial distance of the hexacopter increases. Another measure of performance is to calculate the normalised classical delay beamformer spectrum, where a score of 1 means that the model perfectly describes the sampled covariance matrix which has been modified to contain only phase information for one source, see \mathbf{U} in Section 5.1. In Figure 7b it is shown that the convergence stage increases the accuracy of the model. In Figure 8, plots are given for the GPS and estimated coordinates of the hexacopter over time and these show how closely the estimated values follow the GPS values.

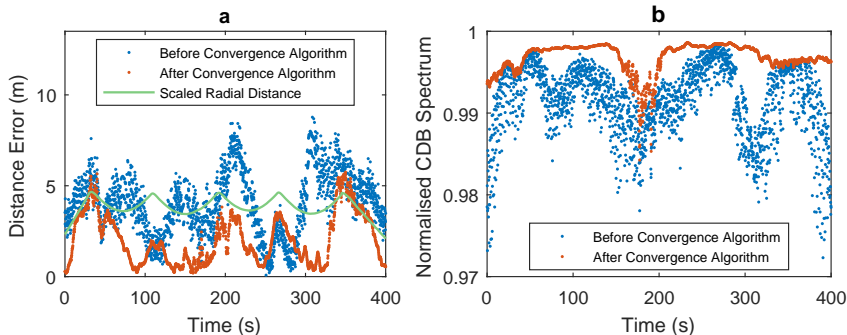


Figure 7. (a) Distance errors before and after the convergence stage for 2000 sample covariance matrices, observed over time. The scaled plot of the hexacopter radial distances has a pattern similar to that of the distance error plots. (b) The normalised CDB spectrum before the convergence stage and after the convergence stage, observed over time

10 Performance Comparison between Proposed Algorithm and 3D MUSIC

To compare the performance of the proposed algorithm to 3D MUSIC, a simulation was performed where the computational time was measured for different search grid sizes. The starting search grid size of $[N_r, N_\theta, N_\phi] = [128, 128, 128]$ was scaled by $\alpha \in [1, 2]$. As expected, the computational time of the 3D MUSIC algorithm increased cubic with search grid size, while the new proposed algorithm increases linearly, see Figures 9a and b, respectively. A significant speed-up of at least 2 orders of magnitude was achieved using a desktop computer with an Intel Core i5-2500k chip, see Figure 9c.

Both 3D MUSIC and the proposed algorithm have the same accuracy, since they both converge to the same peak, see Figure 9d. The lower resolution of the CDB is not a concern, since the preprocessing in stage 1 separates the RFI sources.

11 Conclusion

A new localisation algorithm for interferometric arrays with low array beam sidelobes is proposed. The algorithm is validated using simulations and has a similar accuracy to the 3D MUSIC algorithm. The advantage of the proposed algorithm is that the computational complexity is reduced from $\mathcal{O}(N_r \times N_\theta \times N_\phi)$ to $\mathcal{O}(N_r + N_\theta + N_\phi)$. The drawback is that the algorithm introduces weighting matrices that have to be calculated once a priori and stored. The method was also applied to uncalibrated data

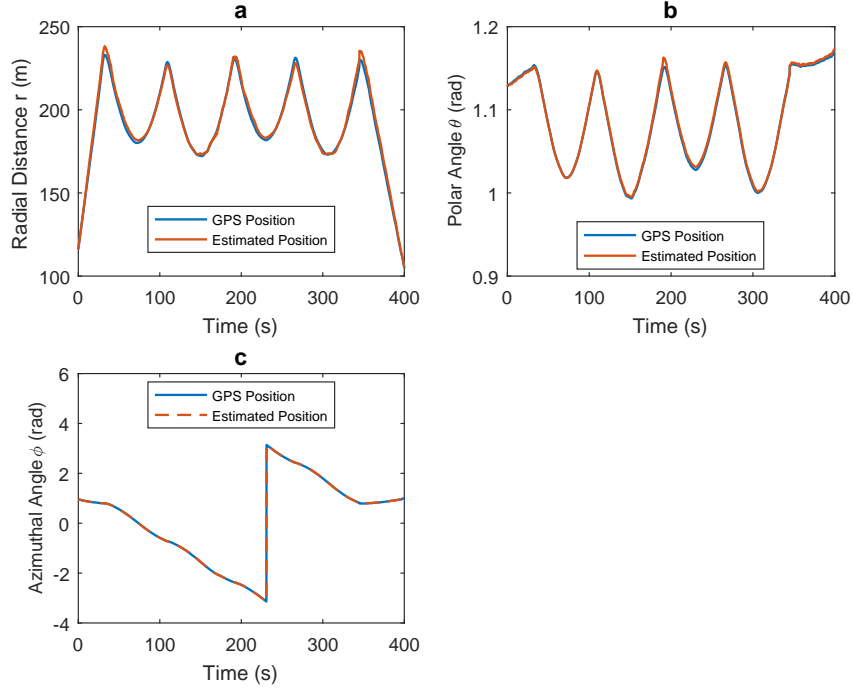


Figure 8. (a) GPS and estimated radial distances of the hexacopter from the array centre, observed over time. (b) GPS and estimated polar angles of the hexacopter from the array centre, observed over time. (c) GPS and estimated azimuthal angles of the hexacopter from the array centre, observed over time.

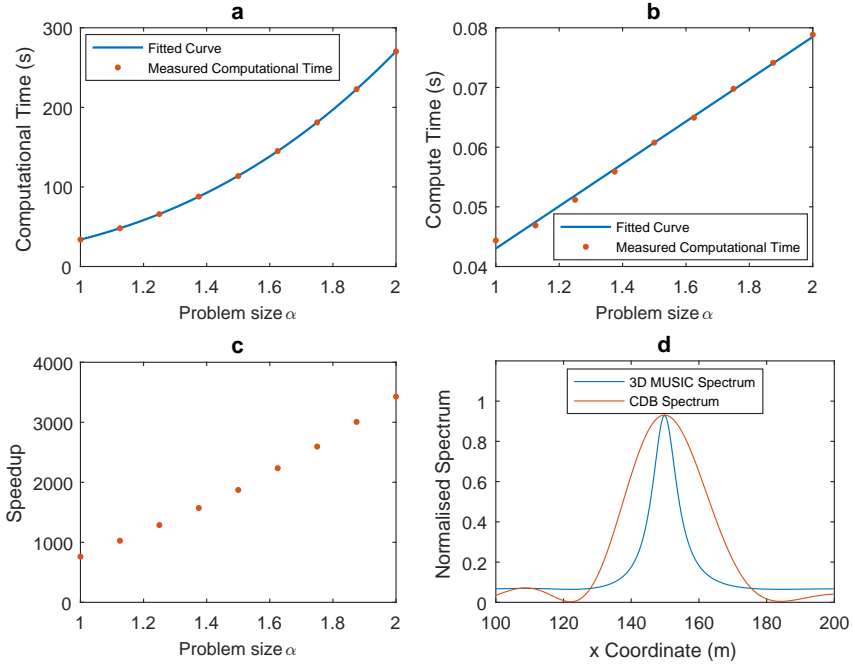


Figure 9. The problem size α is the factor by which the resolution is increased. (a) Computational time using the 3D MUSIC algorithm with a fitted cubic polynomial. (b) Proposed algorithm with a fitted straight line. (c) Speedup of proposed algorithm relative to 3D MUSIC. (d) Normalised spectra for CDB and 3D MUSIC with y and z coordinates fixed for data from the hexacopter measurement, see Section 9.

generated by a LOFAR station while a hexacopter was flying around the array and broadcasting a continuous-wave signal. For this data, the mean distance between the estimated positions of the hexacopter and the corresponding real positions is 2 m (with mean absolute deviation of 1.16 m) which is less than the wavelength of 6.7 m. These results clearly demonstrate the accuracy and precision of the proposed algorithm to locate RFI sources.

Acknowledgments

This work is funded and supported by IBM, ASTRON, the Dutch Ministry of Economic Affairs and the Province of Drenthe, SKA South Africa, the South African Research Chairs Initiative of the Department of Science and Technology, the National Research Foundation of South Africa, and the Netherlands Organisation for Scientific Research. Data and Matlab code can be found at <https://www.dropbox.com/sh/qiea2tck9vtqonq/AACPfMEzd1bY3aVN1WCBg0d8a?dl=0>.

References

- Balanis, C. A., and Ioannides, P. I. (2007). *Introduction to Smart Antennas*, Morgan & Claypool Publishers.
- Bolli, P. et al. (2017). In-Situ Characterization of International Low-Frequency Aperture Arrays by Means of an UAV-based System, *URSI General Assembly and Scientific Symposium (URSI GASS)*, Montreal (Canada).
- Challa, R., and Shamsunder, S. (1995). High-Order Subspace-Based Algorithms for Passive Localization of Near-Field Sources, *Proceedings of ASILOMAR-29*, 2, 777–781, doi:10.1109/ACSSC.1995.540806.
- Grosicki, E., Abed-Meraim, K., and Hua, Y. (2005). A Weighted Linear Prediction Method for Near-Field Source Localization, *IEEE Transactions on Signal Processing*, 53, 10, 3651–3660, doi:10.1109/TSP.2005.855100.
- Huang, Y. D., and Barkat, M. (1991). Near-field Source Localization by Passive Sensor Array, *IEEE Transactions on Antennas and Propagation*, 39, 7, 968–975, doi:10.1109/8.86917.
- Hung, H., Chang, S., and Wu, C. (1996). 3-D MUSIC with Polynomial Rooting for Near-field Source Localization, *ICASSP*, 6, 3065–3068, doi:10.1109/ICASSP.1996.550523.
- Sardarabadi, A. M., van der Veen, A., and Boonstra, A. (2015). Spatial Filtering of RF Interference in Radio Astronomy Using a Reference Antenna Array, *IEEE Transactions on Signal Processing*, 64, 2, 432–447, doi:10.1109/TSP.2015.2483481.
- Sardarabadi, A. M. (2016). Covariance Matching Techniques for Radio Astronomy, *PhD Thesis, Delft University of Technology*, doi:10.4233/uuid:3eb46b5b-126c-4d95-8821-fb71ce404cac.
- Starer, D., and Nehorai, A. (1994). Passive Localization of Near-Field Sources by Path Following, *IEEE Transactions on Signal Processing*, 42, 3, March 1994, pp. 677–680, doi:10.1109/78.277864.
- Thompson, A. R., Moran, J. A., Swenson Jr., G. W. (2004). Interferometry and Synthesis in Radio Astronomy Second Edition, *WILEY-VCH Verlag GmbH & Co. KGaA*, doi:10.1002/9783527617845.
- van der Tol, S., and van der Veen, A. (2005). Performance Analysis of Spatial Filtering of RF Interference in Radio Astronomy, *IEEE Transactions on Signal Processing*, 53, 3, 896–910, doi:10.1109/TSP.2004.842177.
- van der Veen, A., Leshem, A., and Boonstra, A. (2004). Signal Processing for Radio Astronomical Arrays, *Processing Workshop Proceedings, Sensor Array and Multichannel Signal*, 1–10, doi:10.1109/SAM.2004.1502901.

- van Haarlem, M. P., et al. (2013). LOFAR: The Low Frequency Array. *Astronomy & Astrophysics*, 556, A2, 1–53, doi:10.1051/0004-6361/201220873.
- Weiss, A. J., and Friedlander, B. (1993). Range and Bearing Estimation Using Polynomial Rooting, *IEEE Journal of Oceanic Engineering*, 18, 2, 130–137, doi:10.1109/48.219532.
- Wijnholds, S. J., Pupillo, G., Bolli P., and Virone, G. (2016). UAV-Aided Calibration for Commissioning of Phased Array Radio Telescopes, *URSI AP-RASC*, 228–231, doi:10.1109/URSIAP-RASC.2016.7601375.
- Yuen, N., and Friedlander, B. (1998). Performance Analysis of Higher Order ESPRIT for Localization of Near-Field Sources, *IEEE Transactions on Signal Processing*, 46, 3, 709–719, doi:10.1109/78.661337.
- Zatman, M. (1998). How narrow is narrowband?, *IEE Proceedings-Radar, Sonar and Navigation*, 145, 2, 85–91, doi:10.1049/ip-rsn:19981670.